TRANSIENT SWASH MOTIONS ON A GENTLY-SLOPING BEACH

Andrea Ruju[1], Javier L. Lara[2], Hervé Michallet[3], Nadia Sénéchal[4], Inigo J. Losada[5]

Abstract

Spectral and wavelet analyses are used to investigate run-up motion on a gently sloping beach with special attention devoted to the coupling between the long-period swash oscillations and the wave grouping outside the surf zone. Run-up elevations were measured under random-wave conditions during the laboratory GLOBEX experiments carried out along a 1:80 sloping, fixed beach. A capacitance wire was deployed parallel to the bottom in order to detect the swash edge. The low Iribarren numbers involved in the experiments led to swash motions dominated by surf beat. High correlation levels between the scale-averaged wavelet power and the run-up suggest that low-frequency swash motions are still associated with the modulation of offshore swell waves. In addition, wavelet analysis supports the idea that swash-swash interactions are important in controlling swash oscillations.

Key words: hydrodynamics, swash, long waves, mild beach, wavelet, laboratory

1. Introduction

On gently-sloping beaches, surf zone processes lead to swash motions dominated by oscillations periods much larger than the peak period of the offshore incoming swell (Guza and Thorton, 1982; Huntley, 1976). In fact, whereas incident swell waves suffer a strong energy damping by breaking processes, the low wave steepness which characterizes long-period waves leads to both small energy losses inside the surf zone and a strong reflection of such low-frequency motions.

Swash oscillations on the beach face are primarily forced by inner surf zone hydrodynamics. Incident broken and unbroken waves penetrate across the surf zone carrying potential and kinetic energy fluxes which are eventually transferred to the swash zone. Kinetic energy is converted into potential energy as waves reach the shoreline and run up the slope; finally they drain back under the effect of gravity. These two reversing phases characterizing a swash event are known as uprush and backwash. Under dissipative conditions, a superposition of swash events is likely to take place with the interaction between seaward-directed and incident flows. These interactions between backwashes and successive uprushes are important since they control swash cycle amplitudes.

Spectral analysis has been extensively used to study the frequency distribution of run-up. It assumes that statistical properties are constant over time, thus providing information representative of global properties of the time series. In fact, the assumption of stationarity, on which spectral analysis relies, precludes the detection of transient features associated with local variations in the time series. An alternative technique that has been developed to evaluate the localized variations of power within a time series is wavelet analysis. Wavelet analysis has been applied to different topics for geophysical research; however, to our knowledge, only one study applied this technique to swash data (Guedes et al., 2011).

It is the objective of this work to integrate the spectral analysis with wavelet analysis to investigate run-up oscillations on a gently sloping beach with special attention devoted to transient feature. In particular, we investigate the coupling between the long-period swash oscillations and the wave grouping outside the surf zone. Moreover, wavelet analysis is applied to address swash-swash interactions effects and their capacity to control run-up oscillations.

[1]School of Marine Science and Engineering, Plymouth University, United Kingdom, andrea.ruju@plymouth.ac.uk
[2]Environmental Hydraulics Institute "IH Cantabria", Universidad de Cantabria, Spain. lopez.jav@unican.es
[3] LEGI, CNRS/G-INP/UJF, BP53, 38041 Grenoble, France. herve.michallet@legi.grenoble-inp.fr
[4]University of Bordeaux, UMR CNRS EPOC, France. N.senechal@epoc.u-bordeaux1.fr
[5]Environmental Hydraulics Institute "IH Cantabria", Universidad de Cantabria, Spain. losadai@unican.es

The paper is organized as follows. Section 2 introduces the wavelet analysis. The laboratory experiments are described in section3. Section 4 illustrates the results for the irregular wave cases. Conclusions are outlined in section 5.

2. Wavelet analysis

Wavelet analysis has been applied in several geophysical investigations for the identification of localized variations of power within a time series by decomposing it into time–frequency space. This section introduces the basic concepts of the wavelet analysis method, an exhaustive description can be found in Torrence and Compo (1998).

It is possible to define the wavelet transform of a time series x, with constant time sampling dt and n=0…N-1, as the convolution of this time series with scaled and translated versions of "mother" wavelet functions ψ(η):

$$W_n(s) = \sum_{n'}^{N-1} x_{n'} \cdot \psi \cdot \left[\frac{(n'-n)dt}{s} \right] \tag{1}$$

where the * indicates the complex conjugate and s is the wavelet scale. The variation in the wavelet scale s and its translation along the time index n allows showing both the energy of any features versus s and how this energy varies with time. The wavelet function ψ(η) depends on a nondimensional time parameter η and must satisfy some conditions among which it must be localized in both time and frequency space and have zero mean. Here, we adopt the Morlet wavelet consisting of a plane wave modulated by a Gaussian envelope:

$$\psi(n) = \pi^{1/4} e^{i\omega_0 n} e^{-n^2/2} \tag{2}$$

where ω0 is a non-dimensional frequency, usually set to 6 to ensure admissibility. The Morlet wavelet function is plotted in figure 1. The wavelet function is normalized to provide unite energy:

$$\psi\left[\frac{(n'-n)dt}{s} \right] = \left(\frac{dt}{s} \right)^{1/2} \psi_0\left[\frac{(n'-n)dt}{s} \right] \tag{3}$$

The normalization procedure allows the comparisons between wavelet transforms (1) characterized by different scales s.

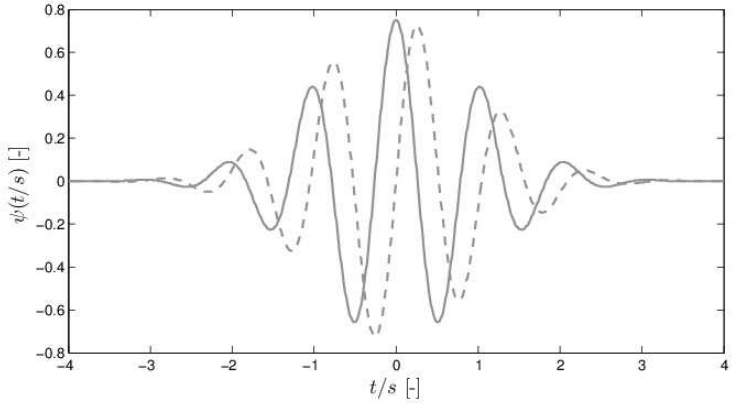

Figure 1 Morlet wavelet function. Solid line: real part; Dashed line: imaginary part.

The wavelet power spectrum can be defined as $|W_n(s)|^2$. For a white-noise process, the expectation value for the wavelet transform is $|W_n(s)|^2 = \sigma^2$, where σ^2 is the variance. By averaging the wavelet spectrum over the entire time series, the global wavelet power spectrum is obtained:

$$\overline{W}^2(s) = \frac{1}{N}\sum_{n=0}^{N-1}|W_n(s)|^2 \tag{4}$$

The global wavelet power spectrum provides an estimation of the true power spectrum of a time series. Once the relationship between the wavelet scale s and the equivalent Fourier period T is calculated analytically for each type of wavelet (for the Morlet wavelet with ω_0=6, T=1.03s), the global wavelet power spectrum is consistent with the corresponding Fourier power spectrum.
The scale-averaged wavelet power is obtained as the weighted sum of the wavelet power spectrum over two specified scales s_1 to s_2:

$$\overline{W_n}^2 = \frac{\delta j \delta t}{C_\delta}\sum_{j=1}^{2}\frac{|W_n(s_j)|^2}{s_j} \tag{5}$$

where δj is the spacing between discrete scales and C_δ is a a constant which for the Morlet wavelet with ω_0=6 takes the value of 0.776. The scale-averaged wavelet power shows the temporal variation of energy associated to a specified band and can be thus used to identify time-dependent features such for example wave groups.

3. Laboratory experiments

3.1. *Wave flume and instrumentations*

The physical experiments, included in the GLOBEX project supported by the European Community's Seventh Framework Programme through the grant to the budget of the Integrated Infrastructure Initiative Hydralab IV, were carried out in the Scheldt flume (The Netherlands). The Scheldt flume is 110 m long, 1 m wide and 1.2 m high. Waves were generated by a hydraulically driven piston-type wave maker located at one side of the flume. Glass sidewalls delimit the lateral boundaries of the flume, except in a 7 m region located in the middle of the flume where concrete sidewalls are present. The fixed bottom profile was made of concrete. A horizontal part of 16.57 m extends between the wave maker and the toe of the slope, then a beach characterized by a gentle constant slope β of 1:80 starts reaching the end of the flume. The still water depth during the experiments was set at 0.85 m in the constant depth section; the undisturbed shoreline lies thus at 84.57 m from the mean position of the wave maker. The bottom profile is shown in figure 2. The origin of the co-ordinate system is fixed at the intersection of the still water level with the wave maker, with the x − z axes positive shoreward and upward, respectively.

Free surface displacements were measured using, respectively, 10 and 12 resistance (RWG) and capacitance (CWG) wave gauges. A capacitance gauge parallel to the beach slope at a height of 0.8 cm above the bottom detected the run-up oscillations on the beach face. Therefore, measured run-up corresponds to the position on the beach face where fluid thickness exceeds 0.8 cm.

The target wave maker motion is provided by a second order wave control signal (van Leewen and Klopman, 1996) in order to reproduce bound subharmonic and superharmonic waves suppressing incident free waves generated at the wave maker. Moreover, active reflection compensation was used to absorb outgoing waves and minimize reflection at the wave maker. By means of experiment repetitions and multiple cross-shore data collections, a total of 190 locations were achieved for wave gauges.

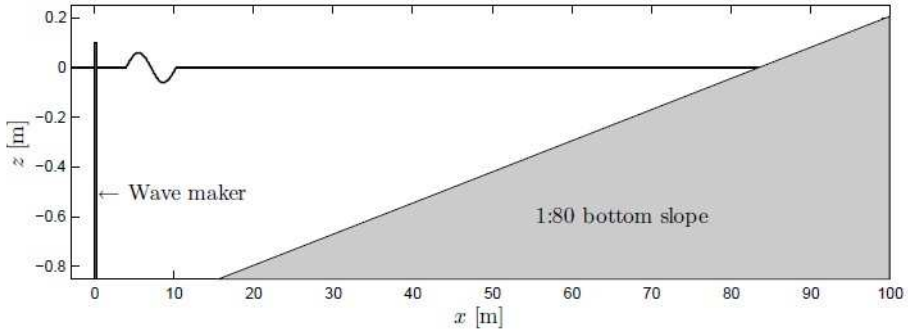

Figure 2. Cross-shore bottom profile and still water level

3.2. *Wave characteristics*

Irregular wave conditions matching a JONSWAP spectrum as well as bichromatic and regular waves were conducted during the laboratory experiments. In this work, only the irregular-wave cases are examined. They are characterized by varying peak frequency (f_p), significant wave height (H_s) and peak enhancement factor (γ). Cases A1 and A3 represent moderate incoming conditions (H_s = 0.1 m), whereas the relatively high H_s of case A2 provides the most energetic conditions (H_s = 0.2 m). Case A3 is characterized by narrow-banded wave spectra (γ = 20) and a relatively large peak period ($T_p = 1/f_p$ = 2.25 s), usually related to clean swells generated by distant storms. Note that, considering the scale factor of 0.05, the significant wave height and peak period ranges in prototype are 2-4 m and 7-10 s, respectively. Table 1 summarizes the three cases with the relative Iribarren number ξ_0 defined as:

$$\xi_0 = \frac{\beta}{\sqrt{H_s / L_0}} \tag{6}$$

where L_0 stands for the wavelength in the generation region calculated with linear theory using the peak frequency of the spectrum.

Table 1. Irregular wave cases.

Case	H_s	f_p	gamma	ξ_0
A1	0.1	0.63	3.3	0.08
A2	0.2	0.44	3.3	0.08
A3	0.1	0.44	20	0.11

4. Results

4.1 Modulation of swash motions by wave groups

The Fourier and the global wavelet power spectra of the incoming free surface elevation are plotted in figure 3 for case A3 (hereinafter, only case A3 results will be presented). The free surface elevation is measured by the most offshore wave gauge located at 6.97 m from the wave maker. The Fourier spectral estimates are obtained by averaging multiple Fourier transforms of 512 s long, 50% overlapped segments sampled at 16 Hz. They are smoothed by merging 3 frequency bands leading to a final frequency resolution of 0.006 Hz. The global wavelet is obtained by integrating the wavelet power spectrum over the entire time series (equation 4). An analogous procedure is adopted to estimate the Fourier and the global wavelet

power spectra of the swash oscillations plotted in figure 4.

Observation of the offshore free surface time series in figure 3 allows the identification of a pronounced wave group modulation. Wave groups are well defined and are constituted by a relatively large number of waves as a result of the high gamma parameter adopted in case A3. In fact, it is wellaccepted that waves with a narrow variance spectral density also have a more pronounced groupiness than broad-banded waves. By comparing the Fourier and the global wavelet power spectra of the incoming free surface elevation, it is possible to conclude that they provide consistent features. Both the location of the peak and the total energy amount are in good agreement. The main difference between the two spectra consists in the shape of the incident peak. In fact, the wavelet peak is wider than the Fourier peak, which results from neighboring wavelet scales being correlated (Torrence and Compo 1998; Guedes et al., 2011).

Run-up on the beach face (figure 4) is dominated by oscillations at surf beat frequency as expected from the relatively low Iribarren number. The swash region extends approximately 3.2 m in the horizontal direction. Both Fourier and global wavelet run-up spectra show no peaks in correspondence of the offshore peak frequency f_p of the incoming waves (see figure 3). The entire sea-swell band and the higher part of the surf beat band are saturated. The saturated region shows a constant slope (in the log-log scale) with an f^{-3} spectral decay consistent with the field experiments of Ruessink et al. (1998) carried out under highly dissipative conditions. The unsaturated low-frequency band of the run-up spectra show no peaks and a good agreement between Fourier and wavelet global spectra can be notified.

Figure 5 shows the incoming wave conditions measured by the most offshore wave gauges. In the upper panel the free surface displacement is plotted, while figures 5b and 5c display the time- and period-dependent wavelet power spectrum and the time-dependent global wavelet power spectrum. The latter is obtained by integrating the wavelet power spectrum over the incident band comprised between the frequencies $f_p/2$ and $6f_p$ (see equation 5). The energy peaks in the wavelet spectrum appear in correspondence of wave group peak and energy is concentrated in a narrow band centered at the peak period 2.25 s. The time-dependent global wavelet power spectrum represents the wave energy history describing the distribution of energy along the time axis. It provides the identification of wave groups making manifest the strong modulation of incoming waves.

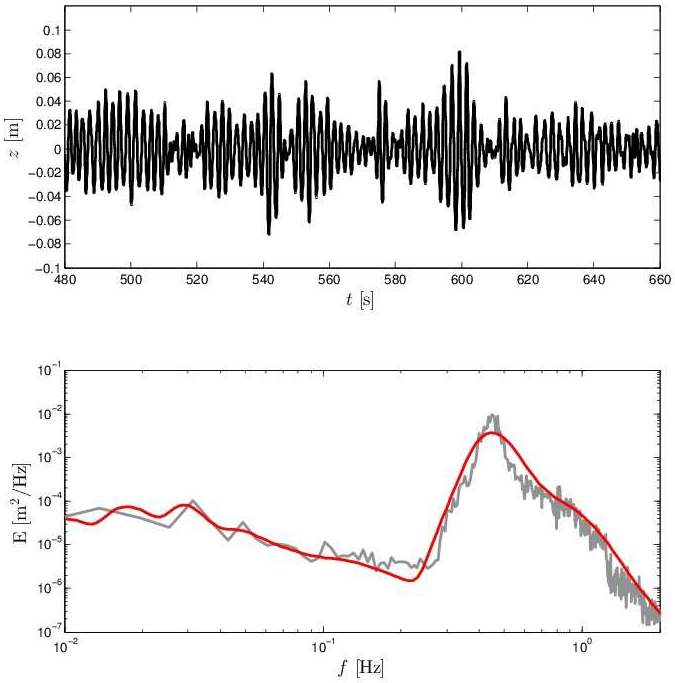

Figure 3. Offshore waves. Upper panel: Free surface time series; lower panel: Fourier (grey line) and global wavelet (red line) power spectra of free surface elevations.

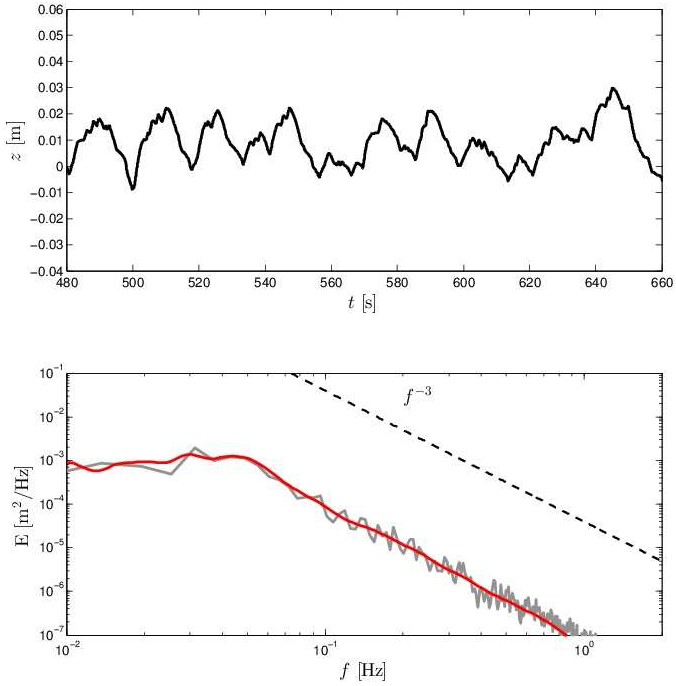

Figure 4. Swash motions. Upper panel: run-up time series; lower panel: Fourier (grey line) and global wavelet (red line) spectra of run-up.

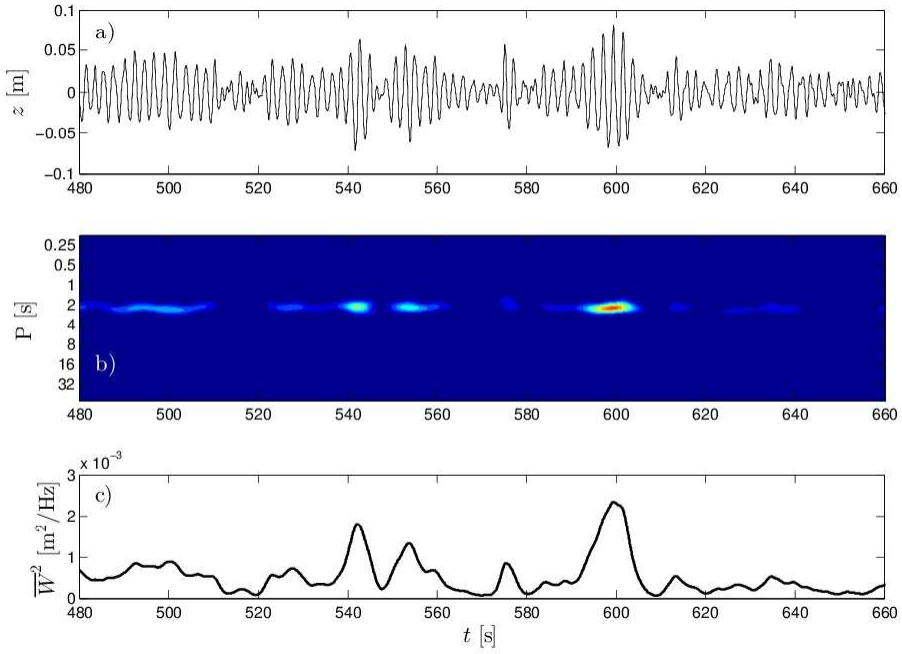

Figure 5. a) Time series of offshore sea surface elevation; b) wavelet power spectrum of the offshore free surface; c) scale averaged wavelet power of the offshore free surface over the incident band.

In order to study the possible coupling between the time variation in incident power associated to wave groups and the long-period swash motions on the beach face, we analyse the spatial evolution of wave

group along the flume. The high spatial resolution of wave gauges throughout the flume length makes it possible to use a quasi-continuous presentation of the scale averaged wavelet power of the offshore free surface over the incident band, as illustrated by the contour plot in figure 6. In the upper portion of the figure the run-up measured by the run-up wire is specified. On the other hand, the offshore wave group modulation is clearly visible in the lower portion where the scale averaged wavelet power of the offshore free surface over the incident band measured at the most offshore wave gauge is shown. The propagation path defined by the group velocity calculated from linear theory using the peak frequency, f_p, (and including set-up) is also illustrated by a white dashed line, its mathematical expression being:

$$F(t,x) = \int_{x_0}^{x} \frac{1}{c_g} dx - (t - t_0) = 0 \tag{7}$$

The values of x_0 and t_0 are chosen in order to superpose the dashed line over the propagation path of the group peak centered at 540 s at the gauge location. The velocity propagation appears to be equal to the group velocity as predicted by linear theory. A strong decrease in peak amplitude owing to the short wave energy dissipation is observed at the breakpoint. Total dissipation of short wave energy in the inner surf zone cancels any leftover of scale averaged wavelet power; no reflection is observed at the shoreline.

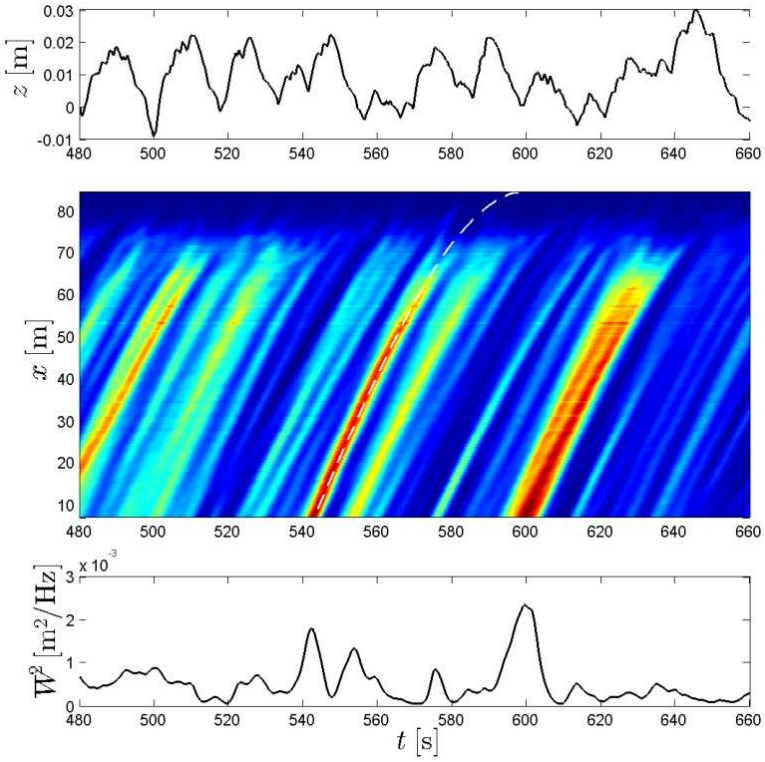

Figure 6. Evolution of wave groupiness along the flume. a) run-up time series; b) scale averaged wavelet power of the free surface along the flume; c) scale averaged wavelet power of the offshore free surface.

The relationship between the offshore wave groups and run-up is investigated by means of a cross-correlation analysis between the scale averaged wavelet power of the offshore free surface and the swash o scillations. The normalized cross-correlation function R between two time series a(t) and b(t) is determined as:

$$R_{ab}(\tau) = \frac{\langle a(t)b(t+\tau)\rangle}{\sigma_a \sigma_b} \tag{8}$$

where the square brackets denote time averaging over the time series length, τ is the ime shift, σ_a and σ_b are the standard deviations of the two time series.

The maximum of the cross-correlation function (shown in figure 7) is found at 48 s which is smaller than the time t_1 required to wave groups to travel from the most seaward gauge until the shore:

$$t_1 = \int_{x_0}^{0} \frac{1}{c_g} dx = 57s \tag{9}$$

in which x_0 is the cross-shore position of the offshore gauge equal to 6.97 m and the group celerity is calculated from linear theory including set-up. Incident wave-groups are about 30 s which is relatively long duration due to the narrow incident wave spectrum. The time shift of the maximum cross-correlation function is thus on the order of one third of the time required by groups to reach the shore. This time difference is consistent with positive run-up maxima forced by low-frequency wave crests generated during the transformation of the incident wave field above the varying bathymetry. In fact, as waves shoal and break in shallow water, the increasing nonlinearity leads to the radiation of shore-directed free long waves which are likely to propagate in front of wave groups. This dynamic set-up is able to modify the incident wave field reducing the dissipation rate of waves propagating in front of the groups where water depth is temporarily increased and a positive current is expected (Janssen et al. 2003; Ruju et al. 2012). As a result, uprush appears mainly driven by incident and low-frequency waves propagating in front of the group.

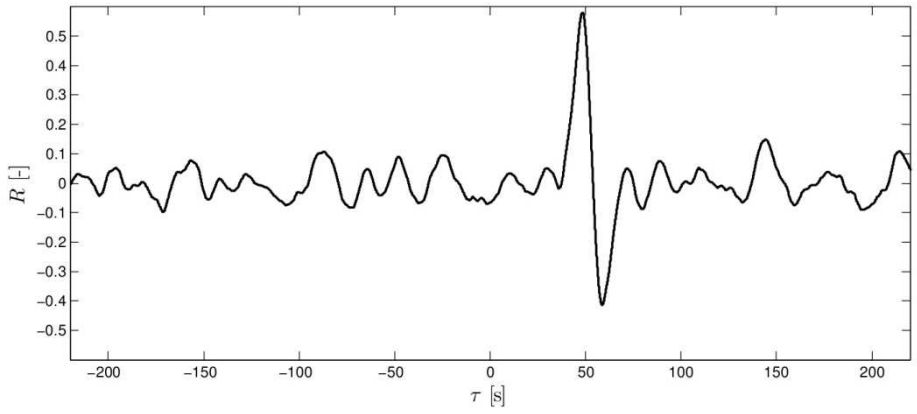

Figure 7. Cross-correlation between the scale averaged wavelet power of the offshore free surface and run-up

The considerable correlation observed between the scale averaged wavelet power of the offshore free surface and run-up supports the hypothesis that long-period swash motions on the beach face are directly coupled with wave groups outside the surf zone. The value of the time shift of the maximum of the cross-correlation function is close to although smaller than the time required to wave groups to reach the shore. This result is consistent with uprush motions driven by waves propagating in front of the groups which travel on the crest of free incident long waves generated during the wave transformation above the sloping bottom.

4.2 Swash-swash interaction

Field observations suggest that swash on gently-sloping beaches is likely to be saturated at sea-swell frequencies (Guza and Thornton, 1982; Holman & Sallenger, 1985) with saturation potentially extending even at infragravity frequencies during highly energetic storms (Ruessink et al., 1998). Saturation implies that an increase of the offshore wave energy would lead to dissipation of wave energy in excess without any growth of run-up oscillations. Energetic incoming wave conditions drive long-period swash oscillations eventually resulting in an overlapping between sequential swash events. This overlap, which

allows interactions between the backwash and uprush phases of swash, is expected to occur when the nondimensional parameter ε_s (Miche 1951) reaches some critical value:

$$\varepsilon_s = \frac{a_s \omega^2}{g\beta^2} \tag{10}$$

in which a_s is the run-up amplitude, ω is the angular wave frequency, g is the gravitational acceleration and β is the beach slope. Field observations provided a value of ε_s in the range 2 to 3 (Huntley at al. 1977). Using the formulation for the swash motion proposed by Shen and Meyer (1963), Baldock and Holmes (1999) re-derived a theoretical value of ε_b (calculated at the limit between inners surf and swash zone) which results in swash saturation and showed that the onset of overlap between sequential swash phases occurs when:

$$H_b \geq \frac{g\beta^2}{4C^2 f^2} \tag{11}$$

where H_b is the incident bore height at the offshore limit of the swash zone, C is a coefficient which describes the efficiency of the bore collapse and takes a theoretical value of 2 and f is the frequency of the incident bores.

Re-arranging equation (11) and using the mean frequency f_m, it is possible to define a parameter P which indicates that swash-swash interactions take place when:

$$P = \frac{H_b 4C^2 f_m^2}{g\beta^2} \tag{12}$$

The wave height and frequency terms in equation (12) can be calculated from the scale-averaged wavelet power and the wavelet power spectrum $|W_n(s)|^2$ at the seaward limit of the swash zone (identified here as the position of the most shoreward gauge that is always wet):

$$H_b = \sqrt{8\overline{W_n}^2} \tag{13}$$

$$f_m = \frac{\sum f |W_n(f)|^2 df}{\sum |W_n(f)|^2 df} \tag{14}$$

in which the wavelet scale s is converted into Fourier frequency f. It is worth notifying that, since both $\overline{W_n}^2$ and $|W_n(f)|^2$ are function of time, the P parameter is time-dependent allowing to track the occurrence of saturation along the time axis.

The upper panel of figure 8 shows the nondimensional P parameter calculated from the time series of the free surface elevation (lower panel) measured at the gauge located at x=84 close to the limit between the inner surf and the swash zone. Figure 8 suggests that swash-swash interactions are important over limited time intervals which roughly correspond to groups of large waves reaching the swash zone. Extending the Baldock and Holmes (1999) reasoning, the time intervals in which overlap between swash events is likely to occur can be identified along the time series. These results support the hypothesis that swash-swash interactions play an important role in controlling swash oscillations and their effect is significant in correspondence of large wave groups reaching the swash zone.

5. Conclusions

In this work, Fourier and wavelet spectral analyses have been carried out in order to identify possible coupling between incoming wave groups and long-period swash motions. The experimental data of swash oscillations have been collected during the GLOBEX experiments involving irregular waves breaking over a gentle-sloping beach. The low Iribarren numbers lead to swash oscillations dominated by long period swash oscillations. The saturated band of the swash spectrum shows a f^{-3} spectral decay.

A cross-correlation analysis between the scale averaged wavelet power of the offshore free surface and the swash oscillations has been conducted. The maximum of the cross-correlation function is found to be smaller than the time required to wave groups to reach the shoreline. This is consistent with uprush motions driven by waves propagating in front of the groups which travel on incident dynamic set-up, thus supporting the hypothesis that long-period swash motions on the beach face are directly coupled with wave groups outside the surf zone.

The surf similarity parameter introduced by Baldock and Holmes (1999) to identify the onset of overlap between sequential swash events has been extended by means of wavelet analysis. A time-dependent parameter is derived in order to identify the saturation as function of time. The results support the hypothesis that swash-swash interactions occur in correspondence of large wave groups reaching the swash zone. Therefore, overlap between sequential swash events seems to be an important factor in controlling large swash oscillations.

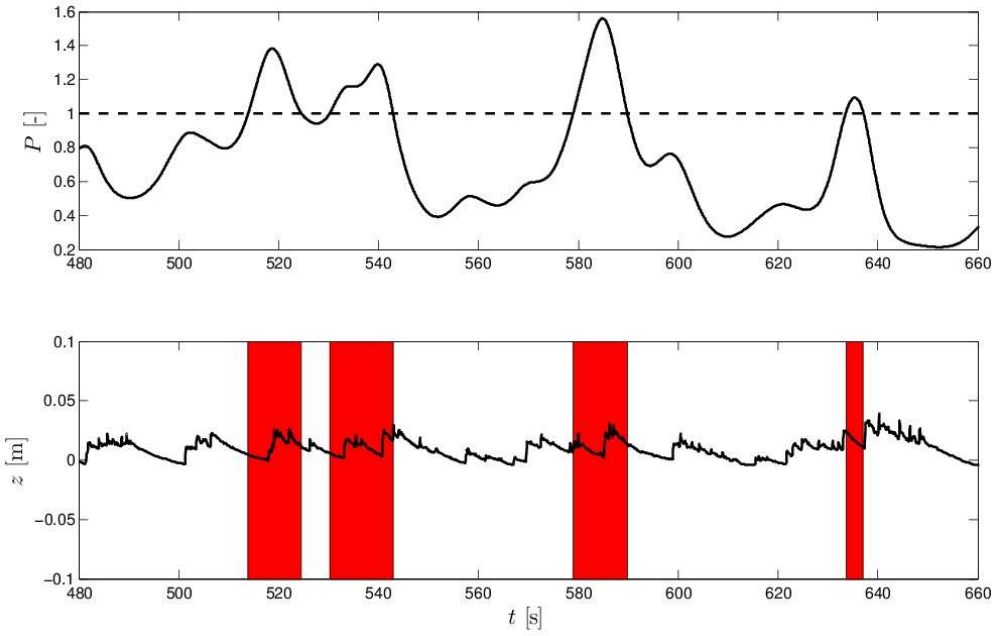

Figure 8. Time series of P parameter (upper panel) and free surface elevation (lower panel) at the seaward limit of the swash zone. The time interval when P exceeds the value of 1 are colored red in the lower panel.

Acknowledgements

Supported by the European Community's Seventh Framework Programme through the grant to the budget of the Integrated Infrastructure Initiative Hydralab IV, Contract no. 261520. The assistance of L. Marcellin (Sogreah-Artelia) in designing the capacitance swash-wire is gratefully acknowledged. The wavelet analysis was performed using codes developed by C. Torrence and G. Compo, available at: http://paos.colorado.edu/research/wavelets/.

References

Baldock, T. and Holmes, P., 1999. Simulation and prediction of swash oscillations on a steep beach. *Coastal engineering*, 36: 219-242.

Guedes, R., Bryan, K. R., Coco, G. and Kruse, S., 2011. Non-stationary patterns in swash motions. *Proceedings of the 20th Australasian Coastal and Ocean Engineering Conference and the 13th Australasian Port and Harbour Conference. Barton, A.C.T.: Engineers Australia*: 274-279.

Guza, R.T., Thornton, E.B., 1982. Swash oscillations on a natural beach. *Journal of Geophysical Research*, 87 (C1): 483–491.

Holman, R. A. and Sallenger, A. H., 1985. Set-up and swash on a natural beach. *Journal of Geophysical Research* 90 :945–953.

Huntley, D.A., 1976. Long period waves on a natural beach. *Journal of Geophysical Research*, 81: 6441–6449.

Huntley, D.A., Guza, R.T., Bowen, A.J., 1977. A universal form for shoreline run-up spectra?. *Journal of Geophysical Research*, 82: 2577–2581.

Janssen, T.T., Battjes, J.A., van Dongeren, A.R., 2003. Long waves induced by short-wave groups over a sloping bottom. *Journal of Geophysical Research*, 108 (C8).

Miche, R. (1951). Le pouvoir reflechissant des ouvrages maritimes exposes a l'action de la houle. *Ann. Ponts Chausses*, 121: 285–319.

Ruessink, B.G., Kleinhans, M.G., and van den Beukel, P.G.L., 1998. Observations of swash under highly dissipative conditions. *Journal of Geophysical Research* , 103: 3111–3118.

Ruju, A., Lara, J., and Losada, I., 2012. Radiation stress and low-frequency energy balance within the surf zone: A numerical approach. *Coastal engineering*, 68: 44–55.

Torrence, C. and Compo G.P. 1998. A practical guide to wavelet analysis, *Bull. Am. Meteorol. Soc*., 79: 61-78.

van Leewen, P. J. and Klopman, G., 1996. A new method for the generation of second-order random waves. *Ocean engineering*, 23: 167–192.